Journal of Alloys and Compounds 752 (2018) 213–219

Contents lists available at ScienceDirect

Journal of Alloys and Compounds

journal homepage: http://www.elsevier.com/locate/jalcom

Insight into the structure and functional application of Mg-doped $Na_{0.5}Bi_{0.5}TiO_3$ electrolyte for solid oxide fuel cells

Yao Lu [a, b], Carlos Alberto López [c], Jie Wang [a, b], José Antonio Alonso [d, **], Chunwen Sun [a, b, *]

[a] CAS Center for Excellence in Nanoscience, Beijing Institute of Nanoenergy and Nanosystems, Chinese Academy of Sciences, Beijing, 100083, PR China
[b] College of Nanoscience and Technology, University of Chinese Academy of Sciences, Beijing, 100049, PR China
[c] INTEQUI, Universidad Nacional de San Luis, CONICET, Fac. Qca., Bqca. y Far. (Chacabuco y Pedernera, 5700), San Luis, Argentina
[d] Instituto de Ciencia de Materiales de Madrid, CSIC, Cantoblanco, 28049, Madrid, Spain

ARTICLE INFO

Article history:
Received 18 December 2017
Received in revised form
27 February 2018
Accepted 3 April 2018
Available online 6 April 2018

Keywords:
Oxygen ion conductor
Electrolyte
$Na_{0.5}Bi_{0.5}TiO_3$
Mg doping
Solid oxide fuel cells

ABSTRACT

$Na_{0.5}Bi_{0.5}TiO_3$ (NBT) and its acceptor-doped perovskites, as lead-free piezoelectric materials before, have been found to be excellent oxygen-ion conductors with potential applications in intermediate-temperature solid oxide fuel cells (SOFCs). Among them, the Bi deficient and B-site Mg doped sodium bismuth titanate ($Na_{0.5}Bi_{0.49}Ti_{0.98}Mg_{0.02}O_{2.965}$, NBTM) exhibits a remarkable oxygen ionic conductivity. Here, we report a structural analysis on NBT and NBTM ceramics using high-temperature *in situ* neutron diffraction (NPD) to gain insight into the effects of Mg doping on ionic conductivity and structure. Both perovskite oxides exhibit two consecutive phase transformations from *R3c* to *P4bm* at ~400 °C and from *P4bm* to $Pm\bar{3}m$ at ~600 °C. The effects of Bi deficiency and Mg substitution on oxygen vacancy concentration and ion displacements are revealed. In addition, a NBTM supported single cell consisting of Ag-NBTM cathode and Ni-NBTM anode is fabricated to evaluate the possibility of its application in intermediate-temperature SOFCs. The structural stability of NBTM is still a major concern that hinders its utilization at high temperature and under reducing atmosphere.

1. Introduction

Oxygen ion conductors have been widely investigated, owing to their technological importance in various applications, such as solid oxide fuel cells (SOFCs), oxygen sensors, pumps, catalysts and oxygen separation membranes, etc. [1–5]. During the past decades, the climate change and energy shortage issues have put on the agenda to develop efficient energy-conversion devices based on these oxygen ion conductors. So far, great efforts have been made to search for oxygen ion conductors, like ZrO_2 [6], CeO_2 [7], $LaGaO_3$ [8], $CeNbO_{4.25}$ [5], and $NdBaInO_4$ [9]. In these materials, oxide-ion conductivity is realized by the migration of oxygen vacancies or interstitial oxygen ions in solid state, which always involves a high activation energy, since the breaking and reconstruction of chemical bonds and migration of oxygen ions in crystal structure are necessary steps. Therefore, these oxygen-ion conductors usually need to work at high temperatures to improve the ionic mobility. Yttrium stabilized ZrO_2 is a stable electrolyte for SOFCs, but it can only shows relatively high conductivity above 800 °C. Doped ceria and $LaGaO_3$ oxides with higher conductivities at intermediate-temperature were developed as alternative electrolytes [7,8], however they contain many kinds of rare metal elements. Recently, Sinclair *et al.* reported that $Na_{0.5}Bi_{0.5}TiO_3$ (NBT) is an oxygen-ion conductor with low sintering temperature and without rare metal elements, which has been considered as a lead-free piezoelectric material before [10]. The oxygen-ion conductivity in the NBT based material could be further enhanced via Bi-deficiency and Mg-doping at Ti site, e.g. $Na_{0.5}Bi_{0.49}Ti_{0.98}Mg_{0.02}O_{2.965}$ (NBTM), which was ascribed to the highly polarized Bi^{3+} cations, weak Bi–O bond and modified oxygen-vacancy concentrations. Its conductivity reaches ~0.01 S cm^{-1} at 600 °C and is comparable to the well-known oxygen-ion conductors $La_{0.8}Sr_{0.2}Ga_{0.8}Mg_{0.2}O_{2.8}$ and $Ce_{0.8}Gd_{0.2}O_{1.9}$. Several works by conducting first principles calculations have tried to reveal the origin of high oxygen ion conductivity, involving phase structure,

* Corresponding author. CAS Center for Excellence in Nanoscience, Beijing Institute of Nanoenergy and Nanosystems, Chinese Academy of Sciences, Beijing, 100083, PR China.
** Corresponding author.
E-mail addresses: ja.alonso@icmm.csic.es (J.A. Alonso), sunchunwen@binn.cas.cn (C. Sun).

https://doi.org/10.1016/j.jallcom.2018.04.037
0925-8388/

defects formations, anions migration, and local atomistic configurations and so on [11–13]. However, there is no experimental evidence to illustrate the adequacy of the highly polarized Bi^{3+} cations to trigger high oxygen ion mobility. Besides, it is still lacking a fundamental understanding of the mechanism of the oxygen vacancy formation and transport properties in NBTM crystal, particularly at elevated temperature. In addition, compared with the two-steps phase transformations of NBT, following the sequence from *R*3*c* to *P*4*bm* at ~400 °C and from *P*4*bm* to $Pm\bar{3}m$ at ~600 °C, the effects of Bi deficiency and Mg substitution on phase structure are still unclear. Importantly, the chemical stability of NBTM material is still a concern, even though the structure is claimed to be maintained by annealing under atmosphere containing a low concentration of H_2 [14].

To address these respects, high temperature *in situ* neutron diffraction investigations on NBT and NBTM ceramics were conducted in this work to accurately determine the concentration, location, coordination, mobility of oxygen vacancies and polyhedral distortion in the crystal lattice. The effects of Bi deficiency and Mg substitution of NBT on oxygen migration and the ion displacements are systematically investigated from NPD data. In addition, the conductivity of NBT *vs* NBTM is evaluated, and a single-cell NBTM-Ag|NBTM|Ni-NBTM is fabricated to assess the chemical stability under H_2/Air gradient at intermediate-temperature.

2. Experimental

The $Na_{0.5}Bi_{0.5}TiO_3$ (NBT) and $Na_{0.5}Bi_{0.49}Ti_{0.98}Mg_{0.02}O_{2.965}$ (NBTM) oxides were prepared by a conventional solid-state reaction procedure. Analytical grade reactants of Na_2CO_3 (99.8%, Sinopharm), Bi_2O_3 (99.9%, Aladdin), TiO_2 (99.9%, Aladdin), MgO (99.9%, Aladdin) were dried at 300, 180, 800, 1000 °C for 8 h, respectively. Stoichiometric amounts of the raw materials were weighed to obtain 0.04 mol NBT or 0.04 mol NBTM each time. They were ball milled with 40 mL ethanol at 400 rpm for 12 h followed by calcination at 800 °C for 2 h after dried at 85 °C overnight. Then the precursors underwent a second ball milling, drying and calcination process under the same conditions. The obtained powders were ground with addition of several drops of 10 wt% PVB/ethanol solution and pressed into disks under uniaxial pressure of 150 MPa. These pellets with a diameter of ~14 mm were sintered in air at 1100–1150 °C for 2 h. Then the pellets were polished to 300 μm in thickness, for single cells construction. The porosity of the sintered electrolyte pellets was evaluated by measuring their relative density using Archimedes method.

Powder X-ray diffraction (XRD) data were collected on a PANalytical X'Pert3 Powder X diffractometer equipped with a PIXcel1D detector with Cu Kα ($\lambda = 1.5418$ Å) radiation with a step of 0.013°. The electrical conductivity of the NBT and NBTM samples were measured by an AC impedance spectroscopy (Zahner E, German) with 10 mV amplitude. Electrodes were applied by coating Ag paste on both sides of the pellets and then calcined at 700 °C for 0.5 h.

For the structural refinements, neutron powder diffraction (NPD) patterns were collected at room and high temperatures in the D2B neutron diffractometer, with $\lambda = 1.594$ Å in the *Institute Laue Langevin* (ILL), Grenoble, France. The patterns were refined by the Rietveld method using the FULLPROF refinement program [15,16]. A pseudo-Voigt function was chosen to generate the line shape of the diffraction peaks. In the final runs, the following parameters were refined: scale factors for the main and impurity phases, background coefficients, zero-point error, unit cell parameters, pseudo-Voigt corrected for asymmetry parameters, positional coordinates, anisotropic thermal factors, and antisite disorder of Na/Bi. The coherent scattering lengths for Bi, Na, Ti, Mg and O were 3.63, 8.532, −3.438 and 5.803 fm, respectively.

The chemical compatibility of NBTM with Ag and NiO was tested by mixing them in a weight ratio of 1:1 and calcined at 800 °C for 2 h, and examined by XRD. The structural stability of NBTM was evaluated by annealing powders in H_2 at 800 °C for 6 h and then examined by XRD. The single cells were prepared by coating the electrode pastes on NBTM electrolyte pellets with a thickness of 300 μm by a screen-printing method. The composite anode and cathode were prepared by mixing NiO and Ag with NBTM in a weight ratio of 6:4, respectively. The anode and cathode slurries were obtained by mixing with a 6 wt% ethylcellulose/terpineol solution as binder and 10 wt% PMMA as pore former. NiO-NBTM slurry was screen printed on one side of the NBTM pellets followed by calcining at 900 °C for 2 h. The Ag-NBTM slurry was screen printed on the other side and calcined at 800 °C for 2 h. The active area of the electrodes is 0.50 cm^2. Ag paste was then painted on the electrode surface and fired at 700 °C for 0.5 h as current collector. Ceramic adhesive was used to seal the single cell on an alumina tube. Humidified H_2 was obtained by bubbling gas through water at 25 °C and fed as fuel to the anode side, while the air was used as oxidant. The water concentration in hydrogen is about 3 vol %.

3. Results and discussion

The initial identification for NBT and NBTM phases was performed from XRD at room temperature (RT). Fig. 1 shows the XRD patterns, which can be indexed to a rhombohedral structure, space group *R*3*c*, as reported previously for NBT [17,18]. It should be mentioned that, even if no visible impurities were observed under the detection threshold of the XRD instrument, there is still a tiny amount of $NaTi_2O_4$ that was identified in the subsequent NPD measurements.

The surface morphologies of NBTM and NBT pellets are presented in Fig. 2. Both samples exhibit a texture characteristic of very dense pellets (Fig. 2a) and no connected pores are observed in the cross-section images, shown in Fig. 2b and d. The porosity of the sintered NBTM and NBT electrolyte pellets are 4% and 5%, respectively. It should be noted that the densification temperature was decreased from 1150 to 1100 °C and the grain size was increased with doping Mg^{2+} at B-sites which indicates that MgO can improve the sintering behaviour of NBT.

Electrical conductivities of the dense NBT and NBTM pellets were measured with AC impedance spectroscopy. The representative AC impedance Nyquist plots for both materials are shown in

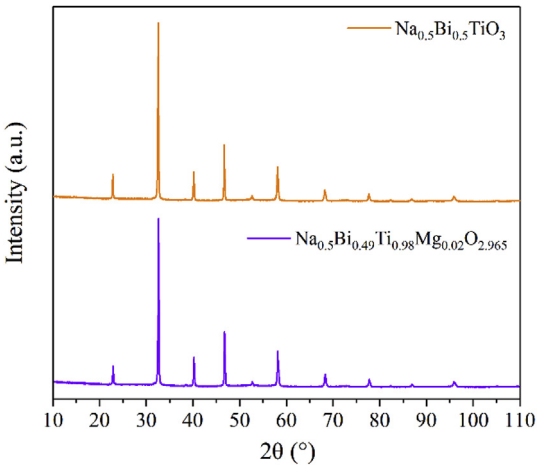

Fig. 1. XRD patterns of NBT and NBTM at room temperature.

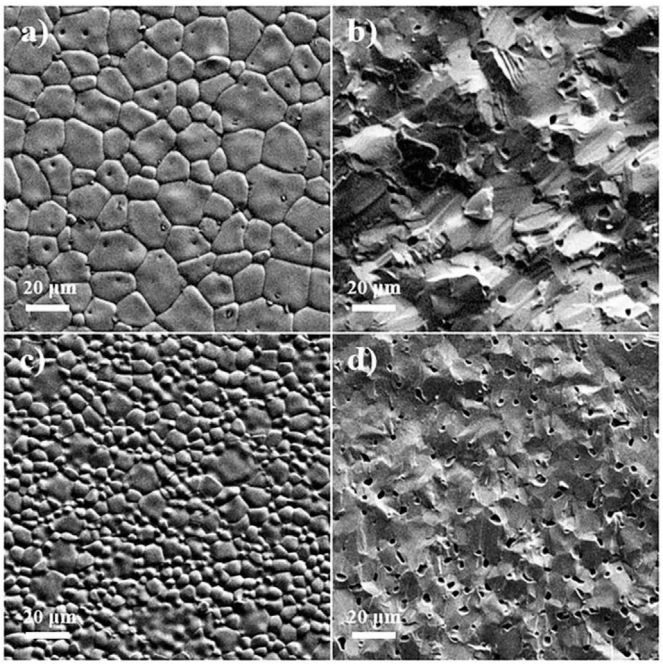

Fig. 2. SEM images of the surfaces and cross-sections of NBTM pellet (a,b) and NBT pellet (c, d) after calcined at 1100 °C and 1150 °C for 2 h, respectively.

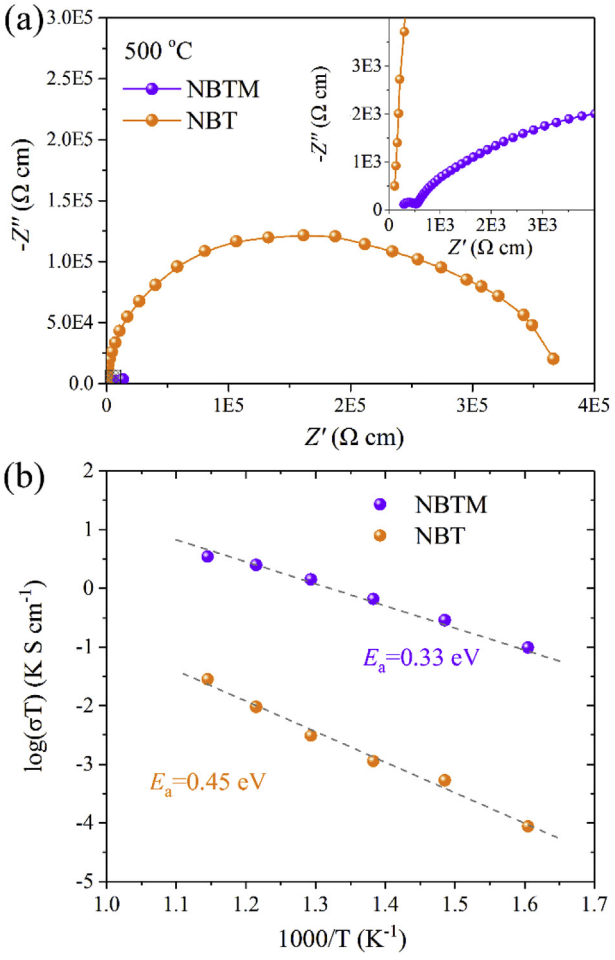

Fig. 3. (a) Representative AC impedance spectra of NBT and NBTM materials at 500 °C. (b) Arrhenius plots of the temperature dependent electrical conductivity of NBT and NBTM materials.

Fig. 3a. Typically, a Nyquist curve contains the arcs, which are usually associated with grain bulk (in the high frequency range), grain boundary (in the intermediate frequency range), and electrode-related impedance response (in the low frequency range). However, due to the frequency limitation of the equipment, the semicircles corresponding to the grain bulk impedance in the high frequency range cannot be measured, while the semicircles at high frequency are assigned to the grain boundary response, according to the fitted capacitance ($C \approx 10^{-9}$ F), as shown in the inset of Fig. 3a. By fitting the curves with Zview software, the total conductivities are calculated and the results are shown in Fig. 3b. The conductivity increases remarkably by doping Mg at Ti site and inducing Bi deficiency. The conductivity reaches 4.0 mS cm^{-1} at 600 °C for NBTM and the calculated activation energy is 0.33 eV, which are consistent with the reported results [19].

A detailed structural characterization (atomic positions, displacement factors, atomic occupancies, etc.) was performed from NPD data in the temperature range from RT to 800 °C. The Rietveld refinements of NPD at RT were successfully performed as rhombohedral in the acentric *R*3*c* space group, obtaining the following unit-cell parameters: $a = 5.4844(2)$, $c = 13.518(1)$ Å and $V = 352.13(3)$ Å^3 for NBT and $a = 5.4869(1)$, $c = 13.524(1)$ Å and $V = 352.59(4)$ Å^3 for NBTM. Despite the similarity of the unit-cell parameters, a subtle increase is observed in the volume cell in the Mg-doped phase. This increase can be assigned to the Mg incorporation at the octahedral Ti positions, given the larger ionic radius of Mg^{2+} (0.72 Å) *vs* Ti^{4+} (0.605 Å) in octahedral coordination. In both cases, the Na/Bi occupation ratios were tested and their values are close to those expected; therefore, in order to avoid oscillations in the refinements, they were fixed to the nominal values.

NBT at high temperatures presents two consecutive phase transitions, as previously reported by Jones et al. [20] The structure is defined in the rhombohedral *R*3*c* space group at RT, and it becomes tetragonal in *P*4*bm* space group at 400 °C, and cubic in $Pm\bar{3}m$ space group at 600 and 800 °C. When the temperature increases, the tilt-system sequences are $a^-a^-a^-$, $a^0a^0c^+$, and $a^0a^0a^0$ for *R*3*c*, *P*4*bm* and $Pm\bar{3}m$, respectively [21]. Fig. 4 shows the excellent agreement between observed and calculated NPD profiles at RT, 400, 600 and 800 °C. The main crystallographic parameters are listed in Tables S1 to S4 for the different temperatures covered in this study.

Fig. 5 illustrates the three crystalline structures observed for NBT, where the cations displacements directions are shown for the non-centrosymmetric space groups. The rhombohedral structure is defined with hexagonal axes and lattice parameters a_H and c_H, and these are related to the pseudo-cubic cell as: $a_H \approx \sqrt{2} \cdot a_{pc}$; $c_H \approx 2\sqrt{3} \cdot a_{pc}$. This non-centrosymmetric space group allows for significant cations displacements along c_H (or $[111]_{pc}$) that explains the ferroelectric behaviour described for this compound. Also, an anti-phase octahedral (TiO_6) rotation in the three directions of the pseudo-cubic perovskite is enabled. As temperature increases, the rhombohedral structure exhibits a transition to a tetragonal unit cell, defined in the *P*4*bm* space group. In this non-centrosymmetric tetragonal system, the unit-cell parameters are related to the pseudo-cubic cell as: $a_T \approx \sqrt{2} \cdot a_{PC}$; $c_T \approx a_{pc}$ and the cationic displacement occurs along c_T (or $[001]_{pc}$), as shown in Fig. 5. Then, at high temperature (600 and 800 °C) a cubic centrosymmetric phase is observed, correctly defined in the $Pm\bar{3}m$ space group, where no octahedral tilts or cations displacements are permitted. Fig. 5 also shows the thermal displacement of Na/Bi cations, described as ellipsoids elongated along the polarization direction. Moreover, a reduction in this elongation is observed as temperature

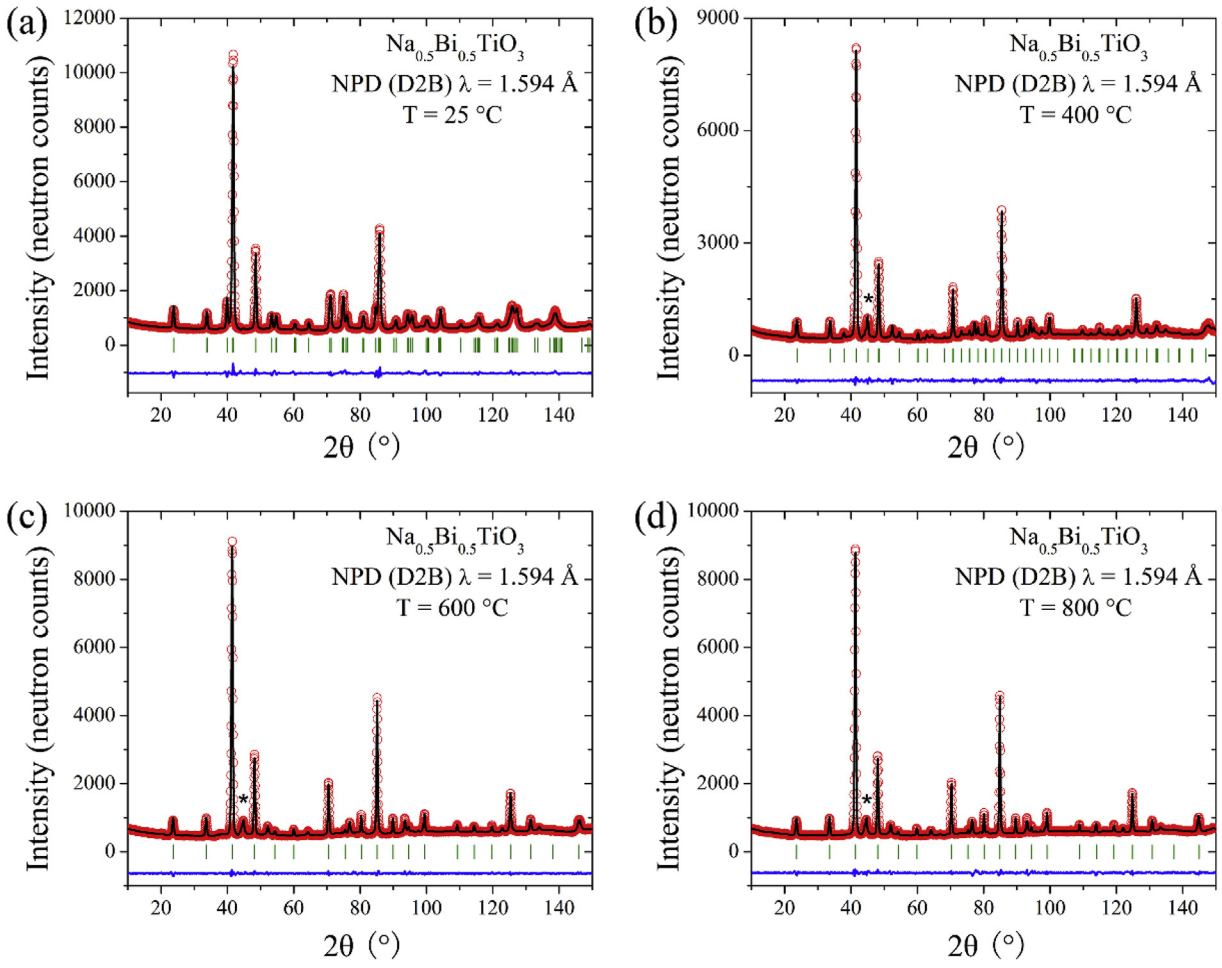

Fig. 4. Observed (circles), calculated (full line) and difference (bottom) Rietveld profiles at a) RT, b) 400 °C, c) 600 °C and c) 800 °C for NBT after NPD refinements. The asterisk corresponds to the main reflection for a metallic phase coming from the components of the furnace.

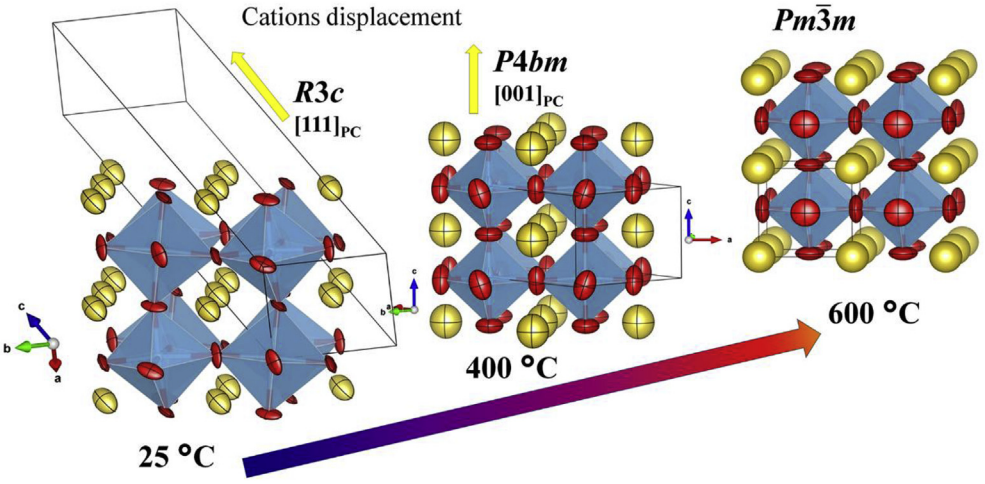

Fig. 5. Schematic views of the three crystal structures observed in the measuring temperature range. Yellow arrow indicates the cations displacement directions in polar space groups. (For interpretation of the references to colour in this figure legend, the reader is referred to the Web version of this article.)

increases (from *R*3*c* to *P*4*bm*), as expected.

NBTM also presents these two phase transitions and exhibits the same phase sequence as NBT; however, a specific behaviour is observed. As temperature increases, the transitions do not develop completely, since a little amount of the rhombohedral phase always remains. At 400 °C, a mixture of *R*3*c*+*P*4*bm* phases is observed and a mixture of *R*3*c*+*Pm*$\bar{3}$*m* phases is observed at 600 and 800 °C. In the pattern of the Mg-doped sample, a little amount (<1%) of $NaTi_2O_4$ was identified. So at all studied temperatures, the impurity $NaTi_2O_4$ was incorporated in the refinement, as previously

mentioned. Fig. 6 shows the good agreement between observed and calculated NPD profiles at RT, 400, 600 and 800 °C for NBTM. As an inset, a pie graph illustrates the percentage amount of each phase for different temperatures. The main crystallographic parameters at different temperatures are listed in Tables S5-8. In these refinements, the cationic Bi^{3+} and anionic O^{2-} vacancies were refined; however, the obtained values are close to the stoichiometric compositions within experimental errors. For this reason, the occupancy factors for Bi^{3+} and O^{2-} were fixed to the nominal values, 0.49 and 1, respectively.

In order to visualize the structural effect of the subtle Mg-doping, several crystallographic parameters were analysed as a function of temperature for NBT and NBTM. A particular effect is observed in the cuboctahedral and octahedral distances of A and B sites, respectively, referred to ABO_3 perovskite. As observed in Fig. 7a, the Mg induces an increase in the octahedral distances (BO_6) and a decrease in the (AO_{12}) cuboctahedra size. These differences are observed at room temperature and at 400 °C (*R3c* and *P4bm*); however at 600 and 800 °C ($Pm\bar{3}m$) the differences are very subtle, probably due to the high symmetry. On the other hand, regarding the oxide mobility behaviour, two crystallographic features were analysed: the atomic displacement factors of oxygen and the area through which the oxygen ions jump from a position to the next. This area is a triangle formed by one B and two A cations in the perovskite ABO_3. These data were analysed in the cubic structures (600 and 800 °C) and they are illustrated in Fig. 7b. These plots show that the area slightly increases upon Mg doping; moreover, the atomic displacements also show an increase of around 10%. These structural features are concomitant with the increase in the ionic conductivity from NBT to NBTM described before (Fig. 3b).

This kind of perovskite oxides has been demonstrated to be a promising oxygen ionic conductor, in the present work and in several recent reports [19,20,22]. Therefore they may find potential applications in intermediate-temperature SOFCs. Consequently, we examined the feasibility of the NBTM as electrolyte for SOFCs. The chemical compatibility of electrolyte with the commonly used cathode materials like Ag, $La_{1-x}Sr_xFe_{1-y}Co_yO_{3-\delta}$, $SmBaCo_2O_{5+\delta}$ and $La_2NiO_{4+\delta}$, as well as the anode material NiO were tested by heat treatment of a mixture of these cathode and anode materials with NBTM at 800 °C for 2 h. The structures of the calcined products were examined by XRD, as shown in Fig. 8a and Fig. S1. It is noted that all the other tested materials exhibited poor compatibility with the NBTM electrolyte except Ag and NiO. While, no impurity phase and peak shift were observed in the XRD patterns of these mixed materials containing Ag and NiO, indicating a good chemical compatibility between them with NBTM at temperatures lower than 800 °C. Therefore, button cells were fabricated consisting of an Ag-NBTM composite as cathode and NiO-NBTM as anode, and tested at 600 and 650 °C with wet H_2 as fuel and air as oxidant. As shown in Fig. 8b, the power density of the cell reaches 2.3 and

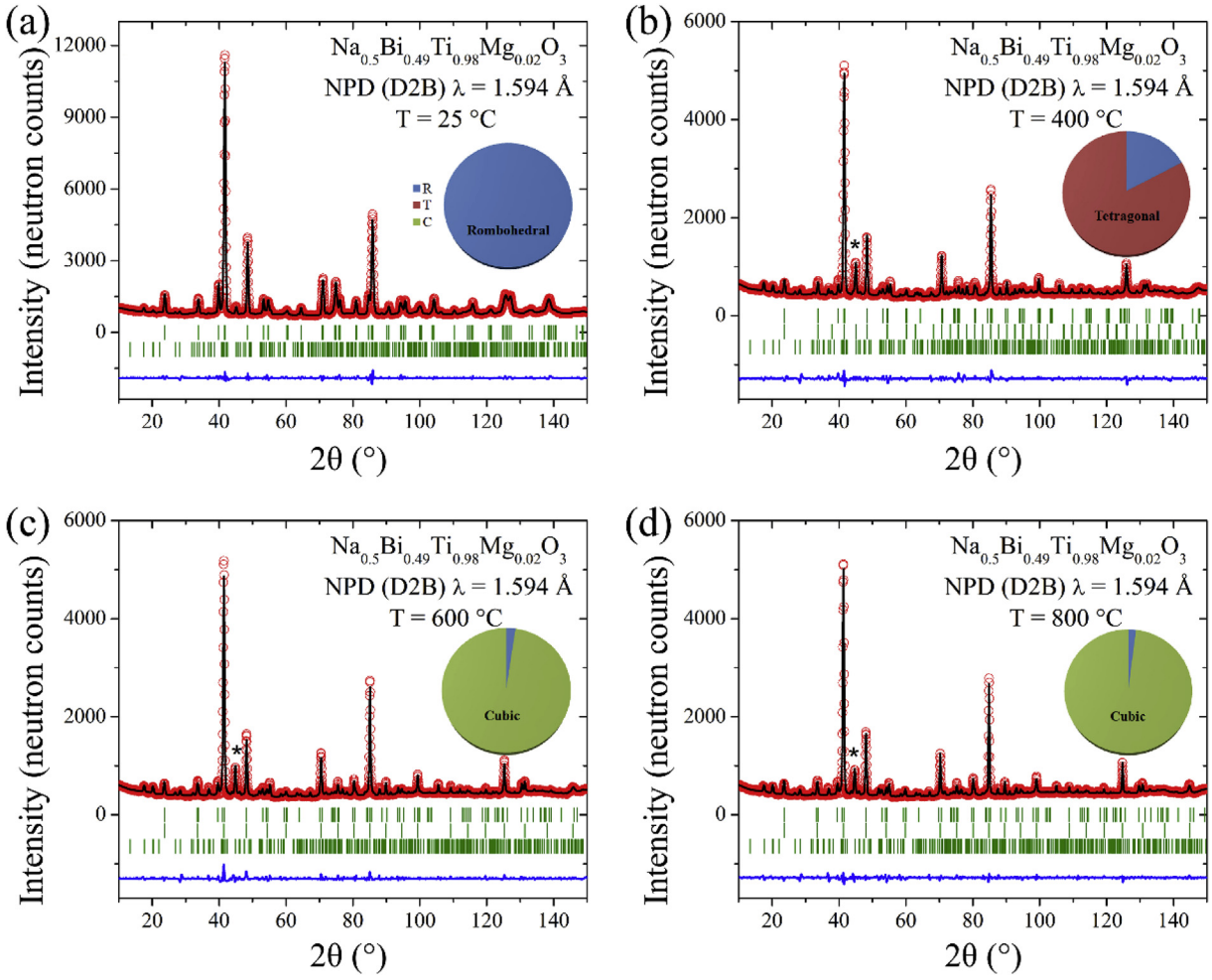

Fig. 6. Observed (circles), calculated (full line) and difference (bottom) Rietveld profiles at (a) RT, (b) 400 °C, (c) 600 °C and (d) 800 °C for NBTM after NPD refinement. The asterisk corresponds to the main reflection for a metallic phase generated by the components of the furnace. Inset: a pie graph indicates the percentage amount of the rhombohedral, tetragonal and cubic phases.

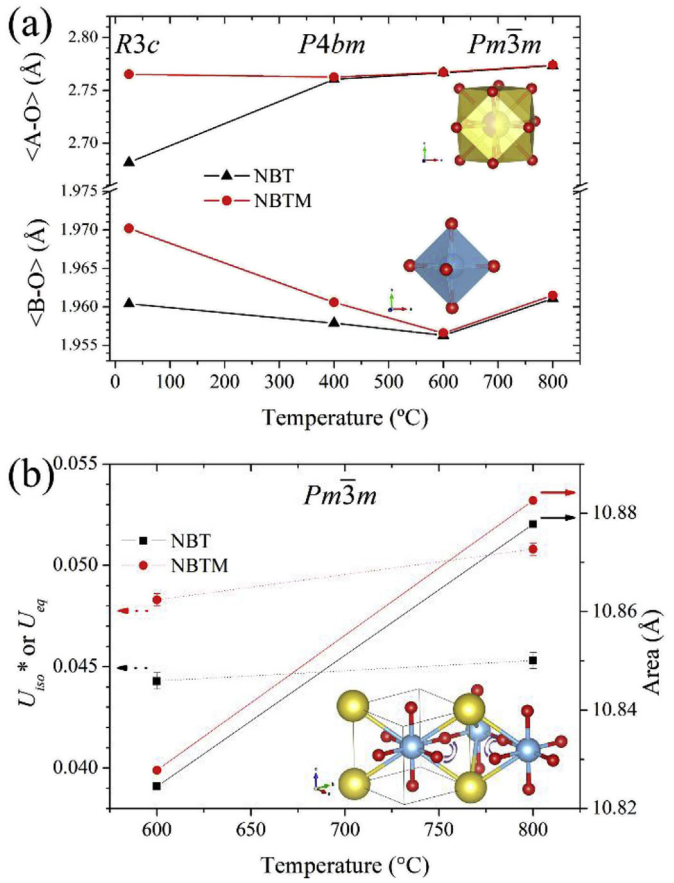

Fig. 7. (a) Thermal evolution of ⟨A–O⟩ and ⟨B–O⟩ distances for NBT and NBTM phases. A and B sites correspond to the ABO_3 perovskite formula. Insets show the shapes of A and B sites. (b) Atomic displacement factors of oxygen and area through which the oxygen ions jump to an adjacent position in cubic phase. The inset shows the schematic view of oxygen jump across the plane formed by one Ti and two Na/Bi cations.

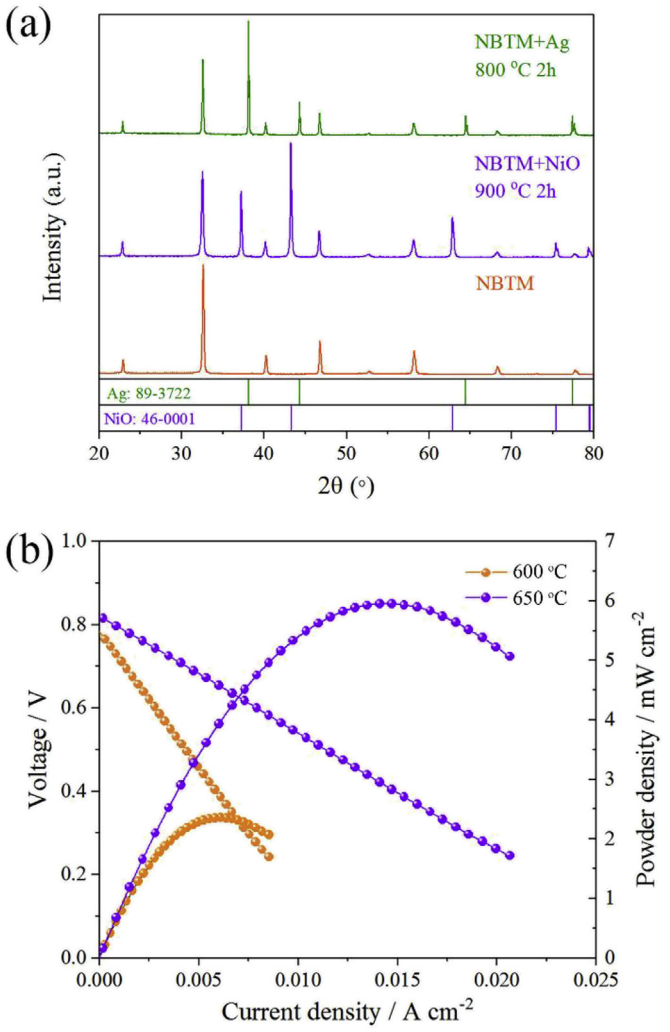

Fig. 8. (a) XRD patterns showing chemical compatibility test of NBTM with Ag and NiO at 800 °C and 900 °C for 2 h, respectively. (b) Voltage and power density versus current density plots for single-cell of NBTM-Ag|NBTM|Ni-NBTM.

6.0 mW cm^{-2} at 600 and 650 °C, respectively. The open circuit voltage of the cell was also lower than those of LSGM based SOFCs in some other published works [23]. It is well known that some materials containing bismuth and titanium cations are reducible under H_2 atmosphere, inducing electronic conductivity and even causing the material decomposition [24–26]. The reduction of Ti^{4+} to Ti^{3+} at low oxygen partial pressure and high temperature has been reported for various titanate perovskites, such as $SrTiO_3$ and $BaTiO_3$, which exhibit n-type electronic conduction based on the release of oxygen as given by the following mechanism [27–29].

$$O_O^{\times} \leftrightarrow V_{\ddot{O}} + 2e^- + \frac{1}{2}O_2 \quad (1)$$

When working in a similar operating environment as SOFCs, the formation of oxygen deficient and electrons following Eq. (1) is the major source of defects. According to the charge neutrality principle, the concentrations of electrons and oxygen vacancies approximately follow the following Eq. (2) [30,31].

$$2[V_{\ddot{O}}] \approx n \quad (2)$$

However, the magnitude orders of electron mobilities are generally larger than those of ionic charge carriers, and thus the electronic conductivity is always predominantly in these titanate perovskites. So, the ionic NBTM electrolyte is possibly changed to a mixed ionic-electronic conductor in intermediate and high temperature ranges at low oxygen partial pressure, thus causing the internal short circuit with low open circuit voltage, as mentioned before.

To further demonstrate whether it is stable under operating conditions in SOFCs, we carried out a chemical stability test in H_2 atmosphere as shown in Fig. 9. It indicates that this kind of NBT-based perovskite oxide was totally reduced and decomposed to other phases in pure H_2 at 800 °C, which is the reason for the poor cell performance. This result suggests that, even though NBTM is a superior oxide-ion conductor, it is not appropriate to be used as an electrolyte in SOFCs.

4. Conclusions

$Na_{0.5}Bi_{0.5}TiO_3$ and $Na_{0.5}Bi_{0.49}Ti_{0.98}Mg_{0.02}O_{2.965}$ perovskites were successfully prepared by a solid-state reaction method. Mg doping at Ti site can improve the sintering behaviour and increase the grain size of NBTM. A rhombohedral structure in the acentric *R*3*c* space group was ascribed by Rietveld refinements from NPD data at RT; due to the larger ionic radius of Mg^{2+} (0.72 Å) *vs* Ti^{4+} (0.605 Å) in octahedral coordination, Mg doping at the octahedral Ti positions increases the lattice parameters. The Mg substitution also induces a

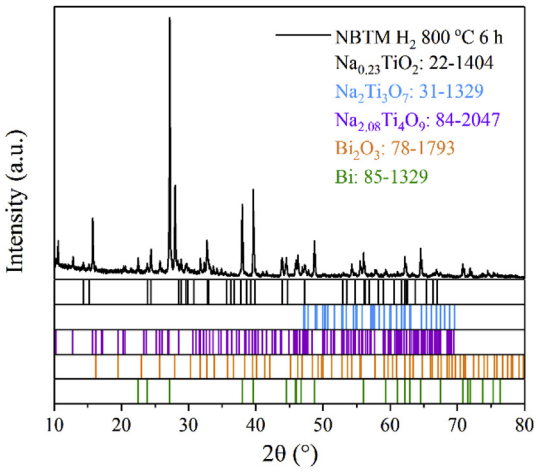

Fig. 9. XRD pattern of the product of treatment on NBTM in H_2 at 800 °C for 6 h, showing the decomposition into several non-perovskite phases, with metallic Bi segregation.

clear increase in the oxygen displacement factor explaining the higher ionic conductivity of NBTM. Both NBTM and NBT also present two phase transitions and exhibit the same phase sequence, from rhombohedral *R*3*c* space group at RT to tetragonal in *P*4*bm* space group at 400 °C, and cubic in $Pm\bar{3}m$ space group at 600 and 800 °C. By contrast with NBT, Mg doping at Ti sites promotes some incomplete phase transformations, observing some *R*3*c* phase in all the temperature range. NBTM exhibits a good compatibility with Ag and NiO; however, a single-cell NBTM-Ag|NBTM|Ni-NBTM based on NBTM electrolyte delivers rather low power density. It is realized that the bad chemical stability of NBTM in reducing atmosphere and compatibility with the most commonly used cathode materials prevents the utilization of this material as electrolyte for intermediate temperature SOFCs.

Acknowledgements

C.S. acknowledges the financial support of the National Natural Science Foundation of China (Nos. 51372271 and 51672029). This work was also supported by National Key R & D Project from Ministry of Science and Technology, China (2016YFA0202702) and the *Thousands Talents Program* for the pioneer researcher and his innovation team in China. C.A. López acknowledges ANPCyT and UNSL for financial support (projects PICT2014-3576 and PROICO 2-2016), Argentine. C.A. López is a member of CONICET. J.A. Alonso thanks the Spanish MINECO for granting the project MAT2017-84496-R, Spain.

Appendix A. Supplementary data

Supplementary data related to this article can be found at https://doi.org/10.1016/j.jallcom.2018.04.037.

References

[1] T. Yang, J. Wang, Y. Chen, K. An, D. Ma, T. Vogt, K. Huang, A combined variable-temperature neutron diffraction and thermogravimetric analysis study on a promising oxygen electrode, $SrCo_{0.9}Nb_{0.1}O_{3-\delta}$, for reversible solid oxide fuel cells, ACS Appl. Mater. Interfaces 9 (2017) 34855–34864.
[2] Y. Lu, H. Zhao, K. Li, X. Du, Y. Ma, X. Chang, N. Chen, K. Zheng, K. Swierczek, Effective calcium doping at the B-site of $BaFeO_{3-\delta}$ perovskite: towards low-cost and high-performance oxygen permeation membranes, J. Mater. Chem. A 5 (2017) 7999–8009.
[3] M.L. Tate, D.A. Blom, M. Avdeev, H.E.A. Brand, G.J. McIntyre, T. Vogt, I.R. Evans, New apatite-type oxide ion conductor, $Bi_2La_8[(GeO_4)_6]O_3$: structure, properties, and direct imaging of low-level interstitial oxygen atoms using aberration-corrected scanning transmission electron microscopy, Adv. Funct. Mater. 27 (2017), 1605625.
[4] S. Fop, E.J. Wildman, J.T.S. Irvine, P.A. Connor, J.M.S. Skakle, C. Ritter, A.C. McLaughlin, Investigation of the relationship between the structure and conductivity of the novel oxide ionic conductor $Ba_3MoNbO_{8.5}$, Chem. Mater. 29 (2017) 4146–4152.
[5] S.S. Pramana, T. Baikie, T. An, M.G. Tucker, J. Wu, M.K. Schreyer, F. Wei, R.D. Bayliss, C.L. Kloc, T.J. White, A.P. Horsfield, S.J. Skinner, Correlation of local structure and diffusion pathways in the modulated anisotropic oxide ion conductor $CeNbO_{4.25}$, J. Am. Chem. Soc. 138 (2016) 1273–1279.
[6] S. de Souza, S.J. Visco, L.C. De Jonghe, Reduced-temperature solid oxide fuel cell based on YSZ thin-film electrolyte, J. Electrochem. Soc. 144 (1997) L35–L37.
[7] Y.J. Leng, S.H. Chan, S.P. Jiang, K.A. Khor, Low-temperature SOFC with thin film GDC electrolyte prepared in situ by solid-state reaction, Solid State Ionics 170 (2004) 9–15.
[8] M. Feng, J.B. Goodenough, K. Huang, C. Milliken, Fuel cells with doped lanthanum gallate electrolyte, J. Power Sources 63 (1996) 47–51.
[9] A. Slodczyk, P. Colomban, S. Upasen, F. Grasset, G. André, Structural stability of anhydrous proton conducting $SrZr_{0.9}Er_{0.1}O_{3-\delta}$ perovskite ceramic vs. proton-ation/deprotonation cycling: neutron diffraction and Raman studies, J. Phys. Chem. Solid. 83 (2015) 85–95.
[10] M. Li, M.J. Pietrowski, R.A. De Souza, H. Zhang, I.M. Reaney, S.N. Cook, J.A. Kilner, D.C. Sinclair, A family of oxide ion conductors based on the ferroelectric perovskite $Na_{0.5}Bi_{0.5}TiO_3$, Nat. Mater. 13 (2014) 31–35.
[11] X. He, Y. Mo, Accelerated materials design of $Na_{0.5}Bi_{0.5}TiO_3$ oxygen ionic conductors based on first principles calculations, Phys. Chem. Chem. Phys. 17 (2015) 18035–18044.
[12] J.A. Dawson, H. Chen, I. Tanaka, Crystal structure, defect chemistry and oxygen ion transport of the ferroelectric perovskite, $Na_{0.5}Bi_{0.5}TiO_3$: insights from first-principles calculations, J. Mater. Chem. A 3 (2015) 16574–16582.
[13] K.C. Meyer, K. Albe, Influence of phase transitions and defect associates on the oxygen migration in the ion conductor $Na_{1/2}Bi_{1/2}TiO_3$, J. Mater. Chem. A 5 (2017) 4368–4375.
[14] F. Yang, H. Zhang, L. Li, I.M. Reaney, D.C. Sinclair, Chem. Mater. 28 (2016) 5269–5273.
[15] H.M. Rietveld, A profile refinement method for nuclear and magnetic structures, J. Appl. Crystallogr. 2 (1969) 65–71.
[16] J. Rodríguez-Carvajal, Recent advances in magnetic structure determination by neutron powder diffraction, Phys. B 192 (1993) 55–69.
[17] J.A. Zvirgzds, P.P. Kapostin, J.V. Zvirgzde, T.V. Kruzina, X-ray study of phase transitions in efrroelectric $Na_{0.5}Bi_{0.5}TiO_3$, Ferroelectrics 40 (1982) 75–77.
[18] E. Aksel, J.S. Forrester, B. Kowalski, M. Deluca, D. Damjanovic, J.L. Jones, Structure and properties of Fe-modified NaBiTiO at ambient and elevated temperature, Phys. Rev. B 85 (2012), 024121.
[19] J. Huang, F. Zhu, D. Huang, B. Wang, T. Xu, X. Li, P. Fan, F. Xia, J. Xiao, H. Zhang, Intermediate-temperature conductivity of B-site doped $Na_{0.5}Bi_{0.5}TiO_3$-based lead-free ferroelectric ceramics, Ceram. Int. 42 (2016) 16798–16803.
[20] G.O. Jones, P.A. Thomas, Investigation of the structure and phase transitions in the novel A-site substituted distorted perovskite compound $Na_{0.5}Bi_{0.5}TiO_3$, Acta Crystallogr. B 58 (2002) 168–178.
[21] A. Glazer, Simple ways of determining perovskite structures, Acta Crystallogr. A 31 (1975) 756–762.
[22] M. Li, H. Zhang, S.N. Cook, L. Li, J.A. Kilner, I.M. Reaney, D.C. Sinclair, Dramatic influence of A-Site nonstoichiometry on the electrical conductivity and conduction mechanisms in the perovskite oxide $Na_{0.5}Bi_{0.5}TiO_3$, Chem. Mater. 27 (2015) 629–634.
[23] H. Sun, Y. Chen, F. Chen, Y. Zhang, M. Liu, High-performance solid oxide fuel cells based on a thin $La_{0.8}Sr_{0.2}Ga_{0.8}Mg_{0.2}O_{3-\delta}$ electrolyte membrane supported by a nickel-based anode of unique architecture, J. Power Sources 301 (2016) 199–203.
[24] J. Berezovsky, H.K. Liu, S.X. Dou, Conductivity and microstructure of bismuth oxide-based electrolytes with enhanced stability, Solid State Ionics 66 (1993) 201–206.
[25] S. Sanna, V. Esposito, J.W. Andreasen, J. Hjelm, W. Zhang, T. Kasama, S.B. Simonsen, M. Christensen, S. Linderoth, N. Pryds, Enhancement of the chemical stability in confined δ-Bi_2O_3, Nat. Mater. 14 (2015) 500–504.
[26] D.P. Fagg, V.V. Kharton, A.V. Kovalevsky, A.P. Viskup, E.N. Naumovich, J.R. Frade, The stability and mixed conductivity in La and Fe doped $SrTiO_3$ in the search for potential SOFC anode materials, J. Eur. Ceram. Soc. 21 (2001) 1831–1835.
[27] R.A. De Souza, Oxygen diffusion in $SrTiO_3$ and related perovskite oxides, Adv. Funct. Mater. 25 (2015) 6326–6342.
[28] M. Ohtaki, M. Ozaki, K. Eguchi, p_{O2}-Dependent nonohmic current-voltage characteristics and current-induced redox behavior of junctioned $SrTiO_3$, J. Electrochem. Soc. 145 (1998) 1165–1173.
[29] N.H. Chan, R.K. Sharma, D.M. Smyth, Nonstoichiometry in undoped $BaTiO_3$, J. Am. Ceram. Soc. 64 (1981) 556–562.
[30] E. Niwa, K. Sato, K. Yashiro, J. Mizusaki, Conductivities and seebeck coefficients of donor-doped-$SrTiO_3$ oxide ceramics, ECS Trans 25 (2009) 2631–2638.
[31] N.H. Chan, R.K. Sharma, D.M. Smyth, Nonstoichiometry in $SrTiO_3$, J. Electrochem. Soc. 128 (1981) 1762–1769.